Key Points:
- We present vertical profiles of water vapor in the Martian atmosphere during global and regional dust storms in 2018-2019
- We show a rapid and significant increase of water vapor in the middle atmosphere (40-100 km) during both global and regional dust storms
- Water vapor reaches very high altitudes, at least around 100 km, during the global dust storm

Correspondence to:
S. Aoki,
shohei.aoki@aeronomie.be

Check for updates

Water Vapor Vertical Profiles on Mars in Dust Storms Observed by TGO/NOMAD

S. Aoki[1,2], A. C. Vandaele[1], F. Daerden[1], G. L. Villanueva[3], G. Liuzzi[3], I. R. Thomas[1], J. T. Erwin[1], L. Trompet[1], S. Robert[1], L. Neary[1], S. Viscardy[1], R. T. Clancy[4], M. D. Smith[3], M. A. Lopez-Valverde[5], B. Hill[5], B. Ristic[1], M. R. Patel[6], G. Bellucci[7], J.-J. Lopez-Moreno[5], and the NOMAD team

[1]Royal Belgian Institute for Space Aeronomy, BIRA-IASB, Brussels, Belgium, [2]LPAP, STAR Institute, Université de Liège, Belgium, [3]NASA Goddard Space Flight Center, Greenbelt, MD, USA, [4]Space Science Institute, Boulder, CO, USA, [5]Instituto de Astrofisica de Andalucia, IAA-CSIC, Glorieta de la Astronomia, Granada, Spain, [6]Department of Physical Sciences, The Open University, Milton Keynes, UK, [7]Istituto di Astrofisica e Planetologia Spaziali, IAPS-INAF, Rome, Italy

Abstract It has been suggested that dust storms efficiently transport water vapor from the near-surface to the middle atmosphere on Mars. Knowledge of the water vapor vertical profile during dust storms is important to understand water escape. During Martian Year 34, two dust storms occurred on Mars: a global dust storm (June to mid-September 2018) and a regional storm (January 2019). Here we present water vapor vertical profiles in the periods of the two dust storms ($Ls = 162$–$260°$ and $Ls = 298$–$345°$) from the solar occultation measurements by Nadir and Occultation for Mars Discovery (NOMAD) onboard ExoMars Trace Gas Orbiter (TGO). We show a significant increase of water vapor abundance in the middle atmosphere (40–100 km) during the global dust storm. The water enhancement rapidly occurs following the onset of the storm ($Ls\sim190°$) and has a peak at the most active period ($Ls\sim200°$). Water vapor reaches very high altitudes (up to 100 km) with a volume mixing ratio of ~50 ppm. The water vapor abundance in the middle atmosphere shows high values consistently at 60°S-60°N at the growth phase of the dust storm ($Ls = 195°$–$220°$), and peaks at latitudes greater than 60°S at the decay phase ($Ls = 220°$–$260°$). This is explained by the seasonal change of meridional circulation: from equinoctial Hadley circulation (two cells) to the solstitial one (a single pole-to-pole cell). We also find a conspicuous increase of water vapor density in the middle atmosphere at the period of the regional dust storm ($Ls = 322$–$327°$), in particular at latitudes greater than 60°S.

Plain Language Summary The most striking phenomenon on Mars is a planet-encircling storm, "global dust storm." Once it starts, the floating dust covers the whole atmosphere for more than several weeks. Recent studies suggest that dust storms effectively transport water vapor from the near-surface to the middle atmosphere. In June to September 2018 and January 2019, a strong global dust storm and a regional storm occurred on Mars, respectively. This study investigates altitude profiles of water vapor in the Mars atmosphere measured during the dust storms, by using brand-new measurements by Nadir and Occultation for Mars Discovery onboard the ExoMars Trace Gas Orbiter. We confirm that the water vapor expanded into the middle atmosphere, and we find that the water vapor reached very high altitudes (up to 100 km) during the dust storms. The dust storms intensify the atmospheric dynamics and heat the atmosphere. As a result, water vapor is lifted to higher altitudes and distributes along the meridional circulation.

1. Introduction

Recent observations and studies have revised our understanding of water loss processes on Mars. The variations of the escape rate are not dominated by the solar extreme ultraviolet (EUV) radiation flux but rather by the variable water vapor abundance in the middle atmosphere (Chaffin et al., 2014, 2017; Clarke, 2018; Clarke et al., 2014; Fedorova et al., 2018; Heavens et al., 2018). Interestingly, these recent measurements imply that global dust storms may effectively transport water vapor from the near surface to the middle atmosphere and hence increase the escape rate with respect to the atmospheric water loss under no-storm conditions. Heavens et al. (2018) and Fedorova et al. (2018) showed the vertical profile of water vapor before/during/after the global dust storm in 2007. They found a significant increase of water vapor abundance in the middle atmosphere and an increase in altitude of the hygropause (where the water content rapidly decreases following saturation and ice cloud formation). Fedorova et al. (2018) found that the

water vapor enhancement is asymmetric between the Northern and Southern Hemispheres—the increase of the water vapor abundance due to the global dust storm is remarkable only in the Northern Hemisphere. This suggests that meridional circulation of the atmosphere is intensified during the dust storms and transports water vapor more efficiently from the Southern to the Northern Hemisphere. Moreover, it is suggested that dust storm related increases of atmospheric temperatures suppress the hygropause, hence reducing ice cloud formation and so allowing water vapor to extend into the middle atmosphere (Heavens et al., 2018; Neary et al., 2019).

To date, vertical profiles of water vapor have been investigated by the solar occultation measurements with Spectroscopy for Investigation of Characteristics of the Atmosphere of Mars (SPICAM) onboard Mars Express (MEX) (Fedorova et al., 2018; Maltagliati et al., 2011; Maltagliati et al., 2013) and by the limb measurements with Compact Reconnaissance Imaging Spectral Mapper (CRISM) and Mars Climate Sounder (MCS) onboard the Mars Reconnaissance Orbiter (MRO) (Clancy et al., 2017; Heavens et al., 2018). The measurements by SPICAM and MCS revealed unexpected high abundance of water in the middle atmosphere that contributes the atmospheric escape of water. They also found that the water vapor abundances in the middle atmosphere are further increased during the global dust storm that occurred in 2007. However, even though it is proposed that an intensified meridional circulation may transport water vapor efficiently, the complete picture of the water vapor distribution during global dust storms is not yet confirmed. This is because (1) the MEX/SPICAM measurements can be performed only in a limited period because the MEX orbit is not dedicated for solar occultation observations, for instance, its measurements during the perihelion season in MY 28 (the year of the previous global dust storm) were performed only during $Ls = 255°–300°$ and no observation is available during $Ls = 200°–255°$ and $300°–360°$ (Fedorova et al., 2018); (2) the previous MRO/MCS analysis (Heavens et al., 2018) did not directly retrieve water vapor vertical profiles from the water vapor spectral features: Water vapor abundances were rather indirectly estimated from the retrieved temperature, pressure, dust, and water ice; and (3) the 2009–2016 MRO/CRISM water vapor profiles, derived from O_2 dayglow profiles, did not encounter global dust storm conditions. In order to understand the mechanism of the water vapor transport from the near-surface to the middle atmosphere, it is crucial to investigate the latitudinal, longitudinal, and temporal variation of water vapor vertical profiles before/during/after global dust storms. Solar occultation measurements by two new spectrometers onboard TGO—NOMAD (Vandaele et al., 2018) and Atmospheric Chemistry Suite (ACS) (Korablev et al., 2018)—are now able to monitor the water vapor vertical profiles through the whole a Martian Year and obtain a latitudinal map for every ~20° of Ls since the orbit of TGO is optimized for solar occultation measurements, producing 24 occultations per day at a maximum (average 5–7 observations per day).

In 2018, for the first time after 2007, a global dust storm occurred on Mars. It lasted for more than 2 months (from June to August). Moreover, following the global dust storm, a regional dust storm occurred in January 2019. TGO began its science operations on 21 April 2018. The NOMAD and ACS observations therefore fully cover the period before/during/after the global and regional dust storms and offer a unique opportunity to study the trace gases distributions during the dust storms. In this paper, we present water vapor vertical profiles from April to September 2018 and from December 2018 to February 2019 retrieved from the NOMAD measurements. We have analyzed those data sets and published two water vapor vertical profiles as early results—one before the global dust storm and the other one during the storm, which present a significantly conspicuous increase of water vapor during the global dust storm (Vandaele et al., 2019). This study presents the results of the extended data sets at the period of the dust storms. The details of the NOMAD observations and the data analysis are described in sections 2 and 3, respectively. The observational results are discussed in sections 4 and 5 for the global dust storm and regional dust storm, respectively. A full general circulation model (GCM) simulation is presented in an accompanying paper (Neary et al., 2019).

2. Observations: NOMAD Solar Occultation

2.1. Instrument—NOMAD Onboard TGO

NOMAD is a spectrometer operating in the spectral ranges between 0.2 and 4.3 µm onboard ExoMars TGO. NOMAD has three spectral channels: a solar occultation channel (SO—solar occultation; 2.3–4.3 µm), a second infrared channel capable of nadir, solar occultation, and limb sounding (Limb Nadir and solar Occultation; 2.3–3.8 µm), and an ultraviolet/visible channel (Ultraviolet and Visible Spectrometer,

200–650 nm). The infrared channels (SO and Limb Nadir and solar Occultation) have high spectral resolution ($\lambda/d\lambda$~10,000–20,000) provided by an echelle grating used in combination with an Acousto Optic Tunable Filter (AOTF) which selects diffraction orders (Neefs et al., 2015). The concept of the infrared channels is derived from the solar occultation in the IR (SOIR) instrument (Nevejans et al., 2006) onboard Venus Express. The sampling rate for the solar occultation measurement is 1 s, which provides better vertical sampling step (~1 km) with higher resolution (~2 km) from the surface to 200 km. Thanks to the instantaneous change of the observing diffraction orders achieved by the AOTF, the SO channel is able to measure five or six different diffraction orders per second in solar occultation mode. One of the most remarkable capabilities of NOMAD is its high spectral resolution in the near infrared range. It allows us (1) to investigate vertical profiles of the atmospheric constituents (such as carbon dioxide, carbon monoxide, water vapor, and their isotopic ratio) and (2) to perform sensitive search of organic species (such as CH_4, C_2H_4, C_2H_6, and H_2CO) and other trace gases (such as HCl, HCN, HO_2, H_2S, N_2O, and OCS) by solar occultation measurements with the SO channel.

2.2. Data Set

In this study, we analyze the solar occultation measurements acquired by the NOMAD SO channel during the period from 21 April to 30 September 2018 (corresponding to $Ls = 162°$–$260°$ in Martian Year (MY) 34) and from 1 December 2018 to 23 February 2019 ($Ls = 298°$–$345°$ in MY 34). Measurements of diffraction order 134 (3,011–3,035 cm^{-1}) and 168 (3,775–3,805 cm^{-1}) are analyzed. Observations of these orders have been regularly conducted since they include strong H_2O bands (both in orders 134 and 168) and CH_4 Q branch (in order 134). In the period above, a total of 987 occultations that operated with both diffraction orders 134 and 168 were acquired. Figure 1 shows the latitudinal coverage of these occultations. As shown in this figure, the latitude shifts from orbit to orbit, at the same time, the longitudinal coverage is dispersed over the whole planet. It demonstrates that this data set allows us to obtain a latitudinal map for every ~20° of Ls. The local solar time is generally around 6 AM or 6 PM outside of the polar regions. Note that the gaps in data between $Ls = 171°$–$179°$, $201°$–$210°$, and $327°$–$333°$ are due to the orbital geometry, which prevents solar occultations from being measured when the orbital nadir track is close to the terminator and the Sun is never occulted by Mars.

2.3. Data Reduction

Solar occultation is a powerful technique for investigating vertical structure of atmospheres. It observes a strong light source—the Sun—through the atmosphere from very high altitude (typically from 250 km altitudes for NOMAD) down to the surface. The absolute calibration of solar occultation spectra is relatively easy since transmittances are obtained by dividing the spectra measured through the atmosphere by the reference solar spectrum recorded outside the atmosphere, which basically removes systematic instrumental effects (except small changes occurring during the occultation). For the calculation of transmittances, we employ the algorithm developed for the reduction of the SOIR data (Trompet et al., 2016). This algorithm does not simply average the spectra recorded outside the atmosphere but calculates its linear regression with altitude for each pixel. The algorithm first calculates the pixel-by-pixel linear regressions with the solar spectra between 150 and 250 km, it then applies them to the spectra between 120 and 150 km where no absorption due to Mars atmosphere is expected. If more than 80% of the transmittances at 120–150 km are equal to one sigma, the algorithm applies the linear regression to the spectra recorded through the Mars atmosphere (below 120 km) and calculates the transmittances. If not, the algorithm recalculates the linear regression by excluding the solar spectrum at the highest altitude. This iterative process continues until accepted. Such a pixel-by-pixel linear extrapolation allows us to reduce the residual instrumental systematic due to small changes during an occultation (such as small deviation of the center wave number of the AOTF transfer function, tiny spectral shift due to grating movement/expansion/contraction because of instrumental oscillations). The instrumental noise is given by

$$(I/F)_{err} = \frac{I}{F}\sqrt{\left(\frac{I_{err}}{I}\right)^2 + \left(\frac{F_{err}}{F}\right)^2}$$

where I is the spectrum through the atmosphere, F is the reference solar spectrum, and I/F is thus the transmittance. The noise in the reference solar spectrum F_{err} is given by the standard deviation of the solar spectra
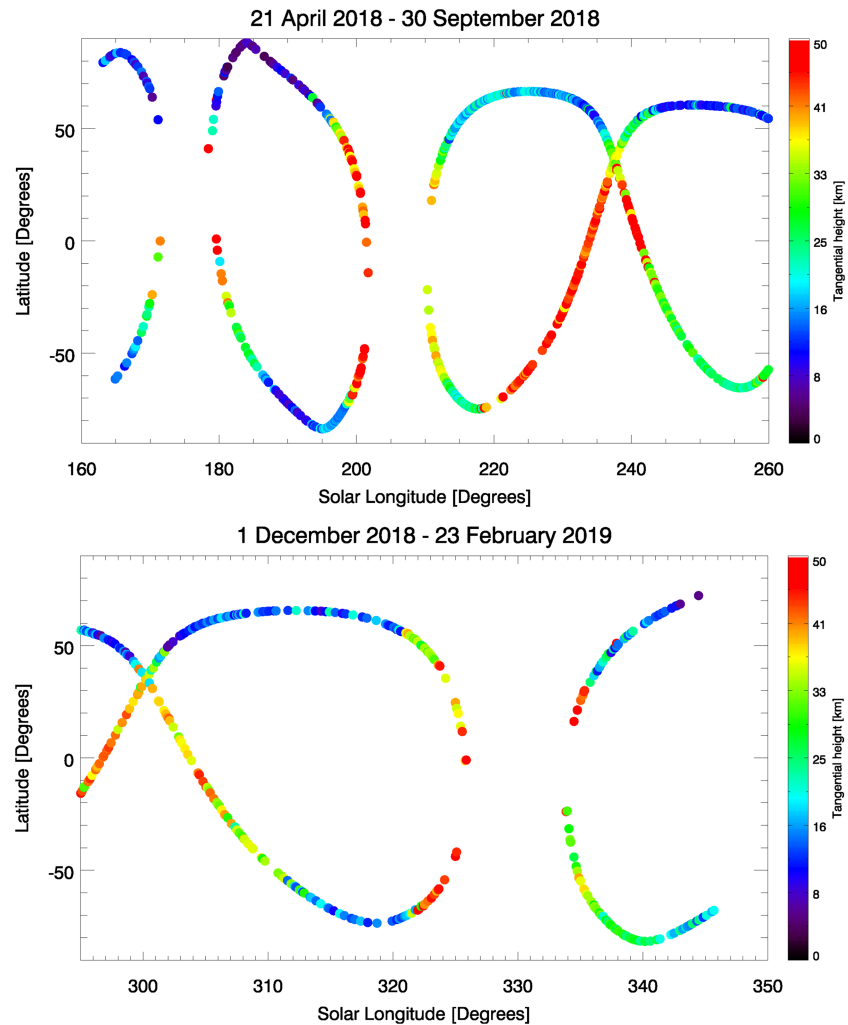
Figure 1. Solar longitude (*x* axis) and latitude (*y* axis) of the solar occultation measurements taken from (a) 21 April to 30 September 2018 and (b) from 1 December 2018 to 23 February 2019 by TGO/NOMAD used in this study. The color denotes the highest altitude at which the mean transmittance of spectra at the diffraction order 168 is less than *exp* (−1.0) (i.e., the optical depth is less than 1.0), which basically corresponds to the top altitude (relatively) free from the dust suspended in the Mars atmosphere.

(normalized) that are used to create the reference solar spectrum. The noise in the spectrum through the atmosphere I_{err} is given by the sum of dark noise (we use the standard deviation of the signal recorded when the radiation reaching the detector is similar to the noise level when the planet is in the line-of-sight (LOS)) and estimated noise from the one in the reference solar spectrum (Vandaele et al., 2013). Typical signal to noise ratio for a single spectrum recorded in diffraction orders 134 and 168 is 1,500–2,500. Figure 2 shows an example of calculated transmittances of the diffraction order 168 during an occultation. When the LOS to the Sun transects the atmosphere, the slant optical depth along the LOS gradually increases owing to the presence of aerosols and molecules, until the atmosphere becomes completely opaque at some tangent altitude. For the particular example in Figure 2, the transmittance drops to zero around 5 km. It usually occurs because of the large amount of dust in the lowermost part of the atmosphere.

2.4. Calibration

Calibration of the NOMAD infrared channels from the first in-flight data was summarized in Liuzzi et al. (2019) and has been improved since then. Based on the work by Liuzzi et al. (2019), in this analysis, the AOTF transfer function of the NOMAD SO channel is characterized as a sinc square function whose side
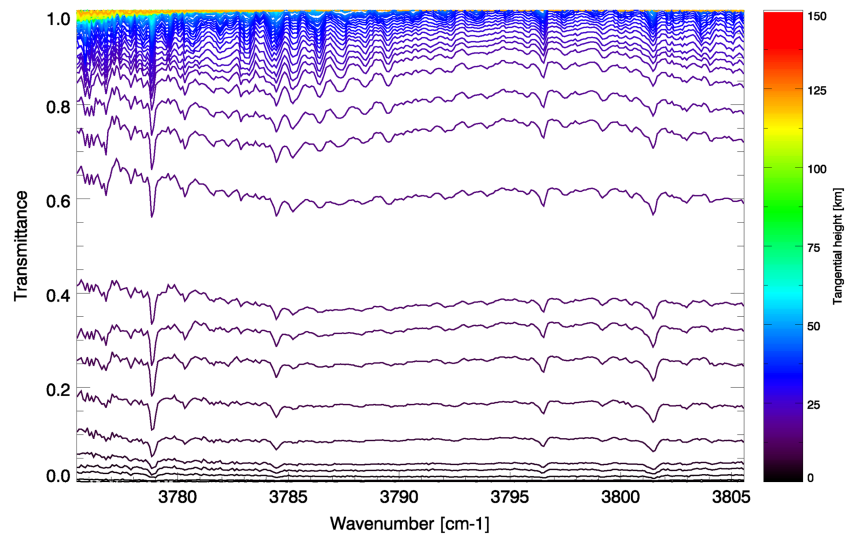
Figure 2. Examples of spectra obtained during one occultation (21 April 2018; the first date of the solar occultation measurements by TGO/NOMAD) in the spectral range between 3,775 and 3,805 cm^{-1} (diffraction order 168). Each transmittance is obtained by dividing the spectra measured through the atmosphere by the reference spectrum recorded outside the atmosphere. The selection of a spectral interval is achieved through the AOTF. The absorption features presented in the spectra are mainly H_2O lines. Differences in colors represent the tangential altitude of the measurements.

lobes are multiplied by 1.3 and 1.8 for diffraction order 134 and 168, respectively. The instrumental line shape is assumed to be a Gaussian function with the full width at half maximum of 0.228 cm^{-1} (λ/$\Delta\lambda$~13,250) for diffraction order 134 and 0.338 cm^{-1} (λ/$\Delta\lambda$ ~11,220) for diffraction order 168. The spectral calibration is first performed based on the results in Liuzzi et al. (2019) and then refined using the solar lines at 3,014.960 cm^{-1} (order 134) and 3,878.865 cm^{-1} (order 168) for each spectrum in the retrieval process.

3. Data Analysis: Retrievals of H_2O Vertical Profiles

3.1. Forward Model

For the forward calculation of the simulated spectra and inversion of the H_2O abundance, we employ the ASIMUT-ALVL radiative transfer code developed at Royal Belgian Institute for Space Aeronomy (Vandaele et al., 2006). The code solves the radiative transfer equation for nadir or solar occultation geometries. It was originally developed for the Earth atmosphere and then extended for Venus (e.g., Vandaele et al., 2008) and Mars (e.g., Vandaele et al., 2019) atmospheres. The code has been widely used in the data analysis of the solar occultation measurements by Venus Express/SOIR.

The radiative transfer calculation is performed in the spectral ranges between ±4 diffraction orders from the main order to properly model the contributions from adjacent orders (Vandaele et al., 2008). CO_2 and H_2O molecules absorption are taken into account in the calculation. The absorption coefficients of CO_2 and H_2O molecules are calculated based on the line-by-line method by using the following spectroscopic database: HITRAN 2016 database (Gordon et al., 2017) for CO_2 and the water line list for CO_2-rich atmospheres by Gamache et al. (2016) for H_2O. A Voigt function is adopted for the line shape function.

The observing geometry is calculated based on the SPICE kernel of the TGO orbits. Based on the geometry (i.e., latitude, longitude, solar longitude, and the local solar time at the tangential point), we extract vertical profiles of the temperature, pressure, and CO_2 volume mixing ratio predicted by the GCM, Global Environmental Multiscale Mars model (GEM-Mars) (Daerden et al., 2019; Neary et al., 2019; Neary & Daerden, 2018). This is performed for each spectrum corresponding to the probed tangent altitude. The modeled atmosphere starts from the tangent altitude of the measurement and up to 150 km altitude with a uniform thickness of 5 km. Note that the tangent altitude is calculated as the shortest distance between the LOS of the center of the field of view and the MGM1025 areoid (i.e., the Mars geoid) (Lemoine et al., 2001). In addition, we note that the atmospheric state predicted by GEM-Mars takes into account the effects of the

dust storms in MY34 (Neary et al., 2019). Neary et al. (2019) described multiple dust storm simulations. We used the run where dust is scaled to the MY34 climatology and the vertical profile was determined using an adjusted Conrath profile (Conrath parameter = 0.0008; GDS0008 simulation).

3.2. Retrievals

We performed the retrieval of H_2O abundance for each spectrum at each tangential altitude independently (Vandaele et al., 2019), that is, using the classical "onion peeling" method. The retrievals start at the top of atmosphere (120 km altitude for this study). At the highest altitude, the initial guess for the H_2O volume mixing ratio is set a small value (typically 1 ppm). Once H_2O absorption features are detected, the retrieved value is used as the initial guess for the next layer below. Since the slant optical depth integrated along the LOS is relatively large for solar occultation measurements comparing to nadir observations, strong H_2O lines (line intensity S larger than ~10^{-20} cm^{-1}/(molecule cm^{-2})) are easily saturated. In our retrieval scheme, if lines are saturated (i.e., the total optical depth at infinite resolution is greater than 1), their weights are reduced as follows:

$$\sigma'(\nu) = \sigma(\nu) \times 10^{\tau(\nu)}$$

where $\sigma(\nu)$ is the instrumental noise, $\sigma'(\nu)$ is the de-weighted error used in the retrievals, and $\tau(\nu)$ is the total slant optical depth integrated along the LOS. Deweighting pixels that contain lines whose optical depth at line center before considering the instrument exceeds 1 would be a strong constraint; however, it is useful to reduce possible biases and uncertainties associated with imperfect knowledge of instrumental functions.

The retrievals are performed using the Optimal Estimation Method (Rodgers, 2000) implemented in a Gauss-Newton iterative scheme. The spectral ranges for the retrieval are the full range of diffraction order 134 (3,011–3,035 cm^{-1}) and a confined spectral range (3,783–3,803 cm^{-1}) for diffraction order 168, where more than 50% of the recorded signal originate from the main diffraction order. This is because the side-lobes in the AOTF transfer function are relatively large for diffraction order 168. Since the side lobes are not yet perfectly characterized, limiting the retrieval to the spectral region where the majority of signal comes from the main order reduces the uncertainties associated with imperfect knowledge of the AOTF function. The free parameters in the retrievals are a factor multiplying the initial guess of H_2O density, and the parameters of the fifth-order polynomial function used to model the continuum of each spectrum. Note that most of the information comes from the sounded tangent altitude (about 70% of the slant number density integrated over the LOS is within 4 km from the tangent height), thus the retrieved local H_2O abundances at the tangential altitudes of the measurements can be considered as its vertical profiles. The continuum established by the polynomial function removes the effect of extinctions due to the presence of aerosols (dust and water ice clouds) along the LOS as well as instrumental features caused by physical changes of the instrument during the occultation (such as small deviation of the center wave number of the AOTF transfer function). Figure 3 shows examples of the fitting results. The intensity of the H_2O lines in the diffraction order 168 is about 100 times stronger (S ~10^{-19} cm^{-1}/(molecule cm^{-2})) than those in the diffraction order 134 (S ~10^{-21} cm^{-1}/(molecule cm^{-2})), which allows us to investigate water vapor abundance from the near-surface to high altitudes. As shown Figure 3b, we firmly detect H_2O with a good signal to noise ratio up to at least 100 km during the global dust storm. The retrievals are conducted for each diffraction order (i.e., 134 and 168) independently in order to evaluate the consistency between orders. Lastly, the vertical profiles of H_2O abundances and their errors are calculated from the weighted averages:

$$W_{134} = \left(\frac{1}{H_2O_{134err}}\right)^2, W_{168} = \left(\frac{1}{H_2O_{168err}}\right)^2$$

$$H_2O = \frac{W_{134}H_2O_{134} + W_{168}H_2O_{168}}{W_{134} + W_{168}},$$

$$H_2O_{err} = \sqrt{\frac{1}{W_{134} + W_{168}}},$$

where $H_2O_{134}, H_2O_{168}, H_2O_{134err}$, and H_2O_{168err} are retrieved H_2O volume mixing ratio and their error values from the diffraction order 134 and 168, respectively.
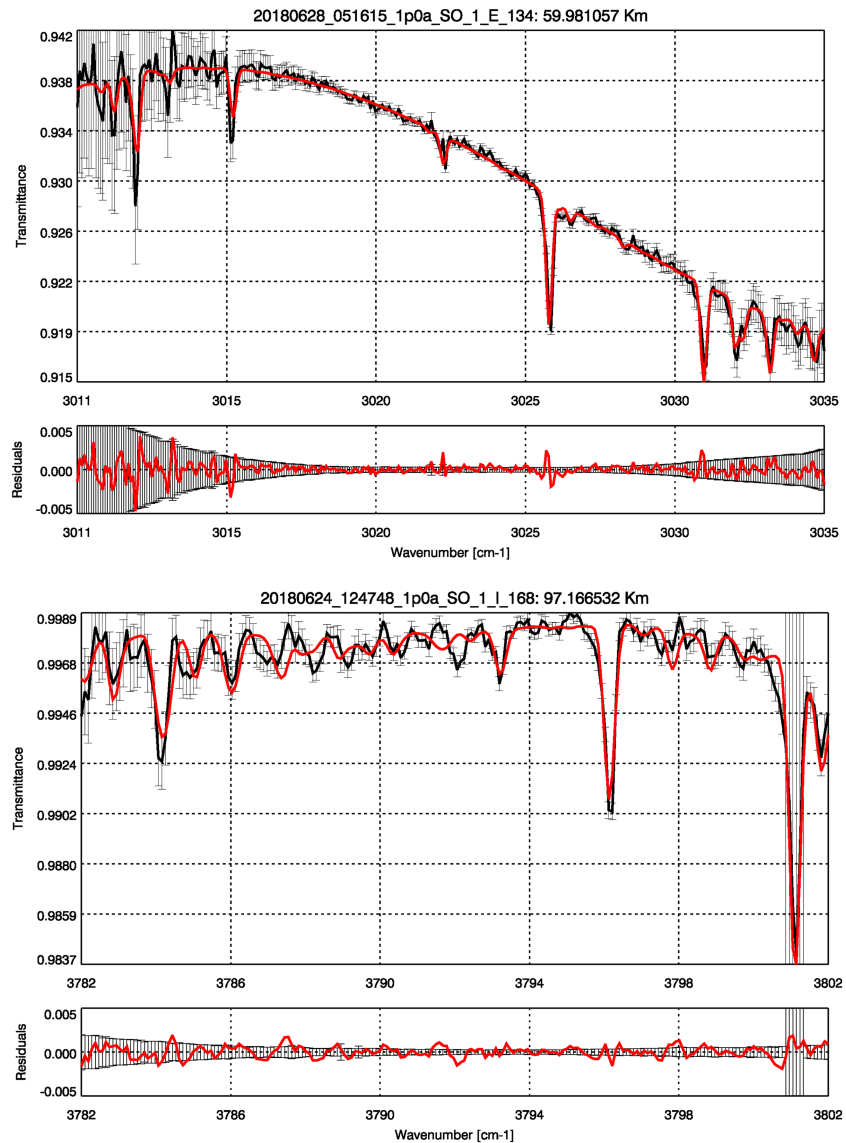
Figure 3. Examples of the data analysis of NOMAD spectra to retrieve H_2O abundance. Spectra of (a) diffraction order 134 taken at 60 km altitude (latitude = 51S°, longitude = 22E°) on 28 June 2018 (Ls = 201°) and (b) diffraction order 168 taken at 97 km altitude (latitude = 38°N, longitude = 138 W°) on 24 June 2018 (Ls = 199°). The black and red curves show the measured NOMAD spectrum and the best-fit synthetic spectrum calculated by the radiative transfer model, respectively. The retrieved H_2O abundance are 201 ($\pm$4) and 233 ($\pm$8) ppm, respectively. The bottom figures show the residuals of the fits in red and the error bars in black. Note that larger residuals around the H_2O line at 3,026 cm^{-1} shown in panel (a) are due to the fact that the spectral calibration is not achieved with a sub-pixel accuracy. The H_2O line at 3,801.4 cm^{-1} shown in panel (b) has larger error bars because the core of the line is saturated.

3.3. Uncertainties

There are three sources of error in the retrieved H_2O volume mixing ratio: (1) instrumental noise on the measured spectra, (2) uncertainty in the vertical temperature and atmospheric density profile used in the radiative transfer calculation, and (3) uncertainty of imperfect knowledge of the NOMAD instrumental functions.

The first error is directly derived from the covariance matrix of the optimal fit parameters in the retrievals. If both diffraction orders 168 and 134 are available, the error values obtained from each diffraction order are weighted averaged, as described above. The median value of this error in the retrievals is about 5%.

The second error can be evaluated by retrievals with temperature profiles shifted by their accuracy. We estimate that the accuracy of the GEM-Mars temperature predictions is about $\pm$10 K. The difference between
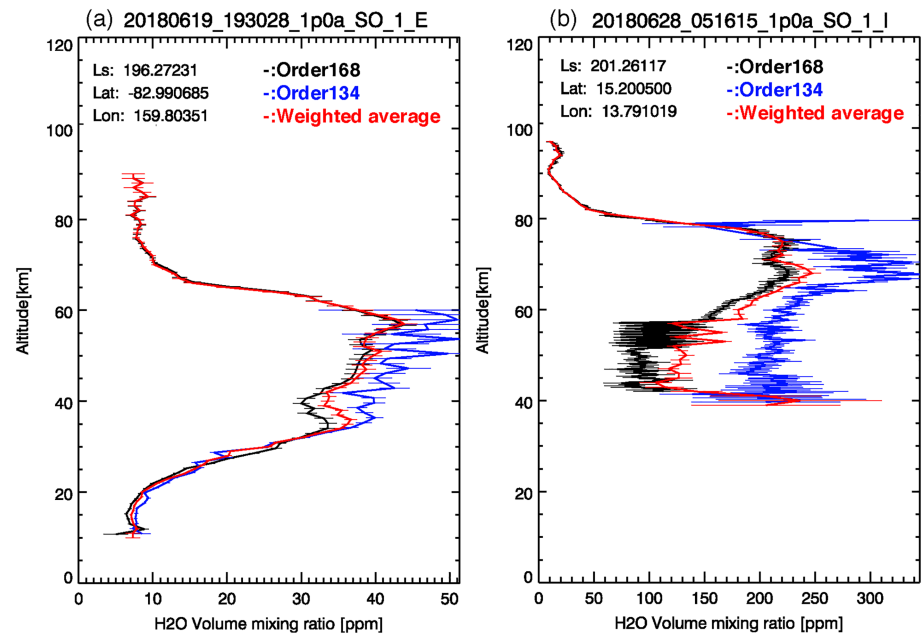
Figure 4. Examples of the water vapor vertical profiles retrieved from solar occultation measurements by TGO/NOMAD taken on (a) 19 June 2018 ($Ls = 196°$, latitude = 82°S, longitude = 159E° at the highest altitude), and on (b) 28 June 2018 ($Ls = 201°$, latitude = 15°N, longitude = 14° at the highest altitude). The black and blue curves show the vertical profiles of water vapor volume mixing ratio retrieved from the spectra in the diffraction orders 168 and 134, respectively. The red curves are their weighted averages. The horizontal bars represent 1σ errors due to the instrumental noise.

the water vapor profiles retrieved with the temperature profiles uniformly shifted by ± 10 K and those with retrieved with the original temperature profiles are about 5%–8%, which can then be considered as the error in the retrieved H_2O volume mixing ratio due to uncertainty in the GEM-Mars temperature. Moreover, since the H_2O volume mixing ratio is the ratio between the water vapor number density and the total atmospheric number density that is based on the predictions by GEM-Mars in this study, the uncertainty in the GEM-Mars total atmospheric number density directly affects the retrieved H_2O volume mixing ratio. We estimate that the accuracy of the atmospheric total number density by GEM-Mars is about 10%–15%; thus, we have another 10%–15% of error in the retrieved H_2O volume mixing ratio.

The third error can be roughly estimated by comparing the retrieved H_2O abundances in each diffraction order (168 and 134). Figure 4 shows examples of the retrieved vertical profiles of the H_2O volume mixing ratio from diffraction orders 134 and 168. The retrieved profiles from each diffraction order are predominantly consistent within 3σ (as shown in Figure 4a); however, the retrieved values are sometimes inconsistent beyond 3σ of the standard retrieval error (as shown in Figure 4b). The median value of the difference between order 168 and 134 retrievals is about twice larger than 1σ of the standard retrieval error, and inconsistent results above 3σ occur in around 35% of occultations. We consider this is mainly due to the fact that instrumental characterization such as the AOTF transfer function is not fully achieved; however, this does not invalidate the conclusions of this study.

4. The Global Dust Storm in 2018

4.1. Overview of the Dust Storm

The global picture of the 2018 global dust storm was summarized in Guzewich et al. (2019) and references therein. The storm started regionally at the middle/end of May (Ls ~180°–185°) across Acidalia Planitia (30°N–60°N, 300°E–360°E) and Utopia Planitia (30°N–60°N, 80°E–140°E). Then, it merged with substantial dust lifting occurring independently in the Southern Hemisphere by the beginning of June (Ls ~190°), and expanded globally by the middle of June (Ls ~195°). This most active period of the global dust storm lasted until the beginning of July (Ls ~205°) and started a long decay phase that ended at the middle of September
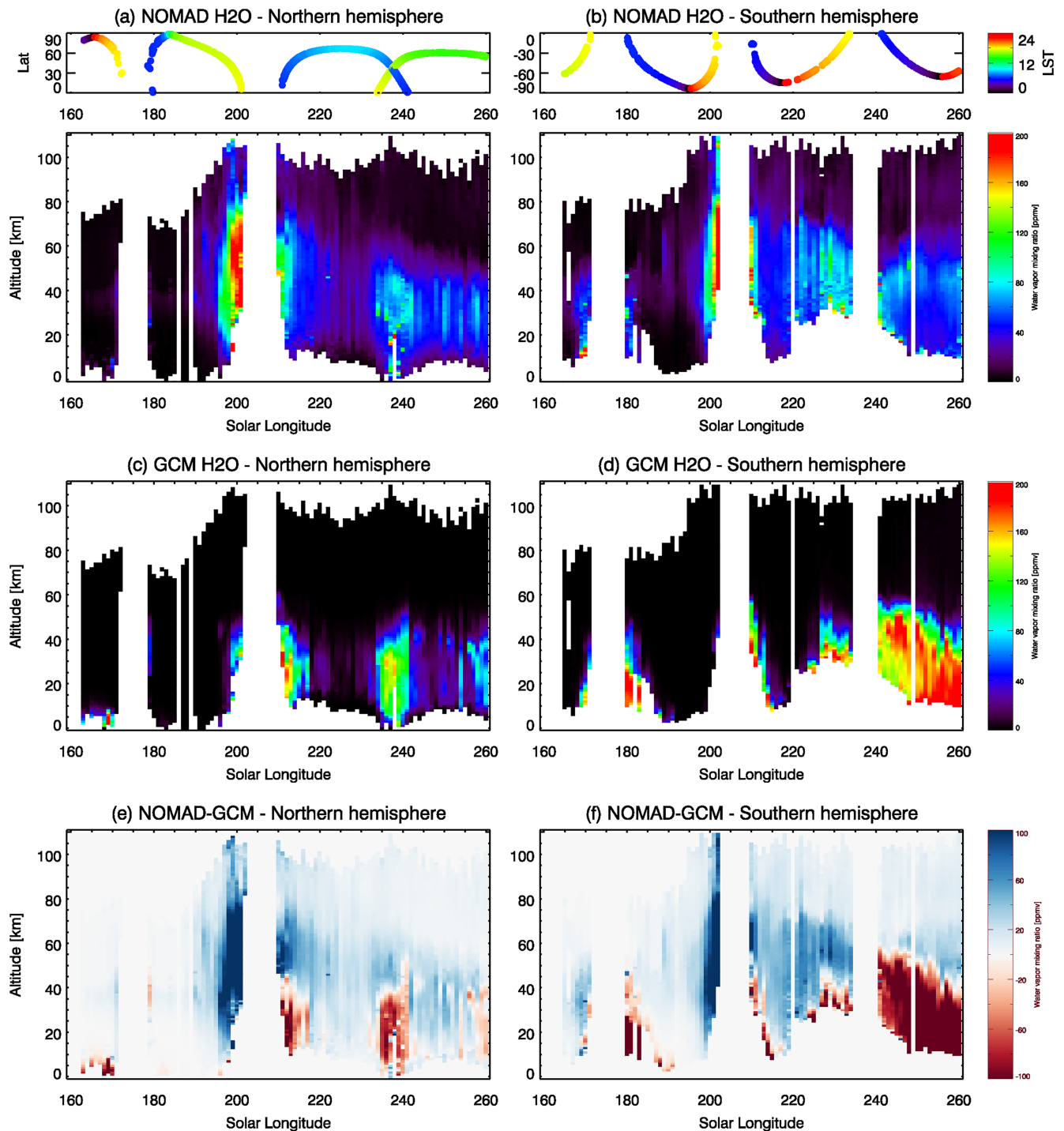
Figure 5. Seasonal variation of the water vapor vertical profiles at $Ls = 162°–260°$ retrieved from the NOMAD data in (a) the Northern Hemisphere and (b) the Southern Hemisphere, (c, d) those predicted by the GEM-Mars for non-dust storm conditions, and (e, f) the differences between the NOMAD retrievals and the GCM predictions. The retrievals and GEM predictions are binned in 1° Ls × 1 km altitude grid (averaged in latitude and longitude). The top panels of (a) and (b) show the latitudes and local solar time of the measurements.

($Ls \sim 250°$). As shown in Figure 1a, the measurements by the NOMAD-SO channels cover the whole period of the global dust storm except for some gaps due to the geometry of the spacecraft's orbit, including the most active period of the dust storm ($Ls = 202°–210°$). The colors in Figure 1a denote the highest tangent altitude at which the slant-optical depth along the LOS is less than 1, which is basically representative of the top

altitude of the most opaque dust region in the atmosphere. The dust top altitudes reach ~50 km in the seasonal range between $Ls = 197°–202°$, which corresponds to the most active period of the global dust storm.

4.2. Seasonal Variation of the Water Vapor Vertical Profiles

Figures 5a and 5b show the seasonal variation of the water vapor vertical profiles at $Ls = 162°–260°$ retrieved from the NOMAD measurements taken in the Northern Hemisphere (Figure 5a) and the Southern Hemisphere (Figure 5b). The top panels show the latitude and local time of the measurements as references. It would be interesting to explore the changes in the water vapor vertical distribution during the 2018 dust storm and for the same period in a non-dust storm year. However, as the 2018 storm occurred in the first year of operations of NOMAD, we have no direct self-consistent reference for the non-dust storm conditions. Previous directly and indirectly retrieved water vapor profiles (see introduction) are sparse and the match in space and time with the NOMAD profiles is in general poor. Therefore, we prefer to use a GCM as tentative reference for the non-dust storm water vapor distribution, as it provides a complete coverage for all times and allows for a full interpolation of the model output to the location and time of all the NOMAD profiles. The vertical water vapor distribution simulated in the GEM-Mars GCM was evaluated by both the water vapor vertical profiles and total water columns retrieved from CRISM in Daerden et al. (2019). Figures 5c and 5d show the same water maps as Figures 5a and 5b but simulated by GEM-Mars for non-dust storm conditions (Daerden et al., 2019). Figures 5e and 5f present the differences between the measured water vapor vertical profiles (Figures 5a and 5b) and the predictions by GEM-Mars for non-dust storm conditions (Figures 5c and 5d).

The abundance of water vapor in the middle atmosphere suddenly increased around $Ls = 190°$ in both hemispheres. This is not seen in the GCM data for non-dust storm conditions (Figures 5c and 5d). In contrast, around $Ls = 210°$, the water vapor abundance in the lower atmosphere seems to have decreased with respect to nondust storm conditions. However, the retrieval accuracy and data coverage is poorer at low altitudes. Also, a comparison of the GCM water vapor profiles with those derived from CRISM (Clancy et al., 2017; Daerden et al., 2019) in non-dust storm conditions shows that the GCM water vapor is too abundant at low latitudes. Therefore, it remains hard to estimate the effect of the dust storm on the behavior of water vapor in the lower atmosphere using the current GCM results. GCM simulations for the MY34 dust storm that reproduce the observed profiles reasonably well are presented in the accompanying paper Neary et al. (2019) and allow for a theoretical assessment of the impact of the dust storm.

The variation of the water vapor abundances occurs very rapidly: The water abundance in the middle atmosphere in both hemispheres increases by an order of magnitude in just a few days (around $Ls = 195°$). Since the timing of this phenomenon corresponds to the onset of the global dust storm and this is not predicted by the GCM for non-dust storm conditions, we conclude that the rapid enhancement of the water vapor in the middle atmospheres is due to the effects of the global dust storm. The water abundances in the middle atmosphere have maximum values around $Ls = 200°$. At that period, we find large water vapor abundances in the middle atmosphere, exceeding 200 ppm. Such large water vapor abundances are similar to MEx/SPICAM observation during the global dust storm in MY 28 (Fedorova et al., 2018). Moreover, we detect water vapor at very high altitude, reaching at 100 km with a volume mixing ratio of ~50 ppm. After these peaks, the enhanced water vapor in the middle atmosphere gradually returned to the typical climatological levels. A small local maximum in water vapor also appears around $Ls = 235–240°$ in the Northern Hemisphere (Figure 5a). This is due to the fact that the measurements are performed at equatorial region where more water vapor is present. While in contrast, the water vapor abundances in the Southern Hemisphere have a small local maximum around $Ls = 230°$, which can be explained by the fact that the water vapor in the Southern Hemisphere does not have a maximum at equatorial but at high latitude (see section 4.3. in detail). Finally, we note that it is difficult to distinguish local time variation from the seasonal one since either sunrise or sunset measurements last for 10°–20° of Ls as shown in the top panel of Figures 5a and 5b.

4.3. Latitudinal Variation of the Water Vapor Vertical Profiles

Figure 6 shows the seasonal variation of latitudinal maps of the water vapor vertical profiles observed by NOMAD (the top panel) and predicted by GEM-Mars for non-dust storm conditions (the bottom panel) during $Ls = 160–195°$ (before the global dust storm; Figure 6a), $Ls = 195°–202°$ (growth phase of the dust storm; Figure 6b), $Ls = 210°–220°$ (mature phase of the dust storm; Figure 6c), $Ls = 220°–240°$, and $Ls = 240°–260°$
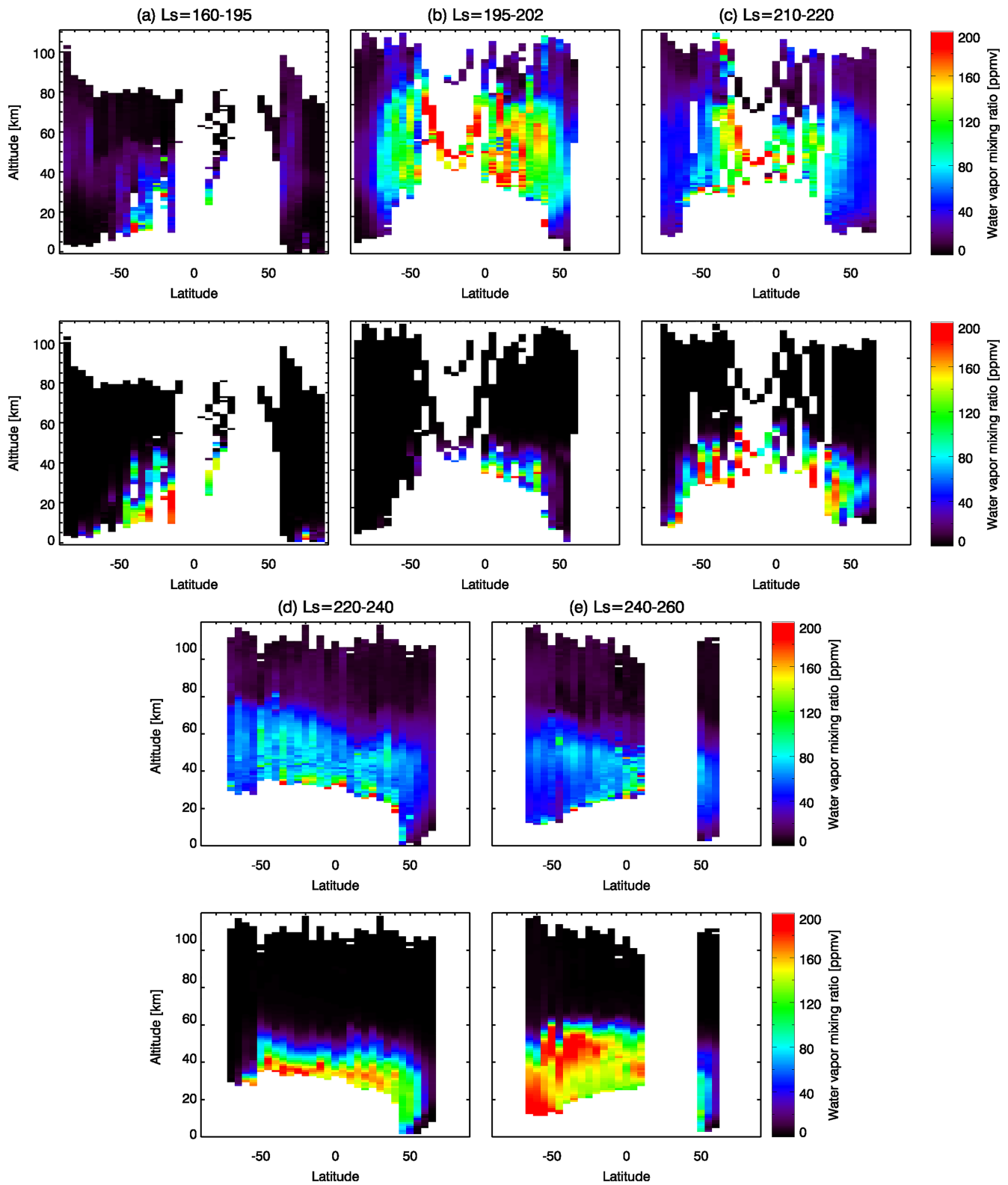
Figure 6. Latitudinal variation of the water vapor vertical profiles retrieved from NOMAD data (the top panels of (a)–(e)), predicted by the GEM-Mars for non-dust storm conditions (the bottom panels of (a)–(e)) in the seasonal range between $Ls = 180°–195°$ (Figure 6a, before the global dust storm), $Ls = 195°–202°$ (Figure 6b, during the growth phase of the storm), $Ls = 210°–220°$ (Figure 6c, during the mature phase of the storm), $Ls = 220°–240°$ (Figure 6d, during the decay phase of the storm), and $Ls = 240°–260°$ (Figure 6e, during the decay phase of the storm). The retrievals and GEM predictions are binned in 5° latitude × 1 km altitude grid (averaged in season and longitude).
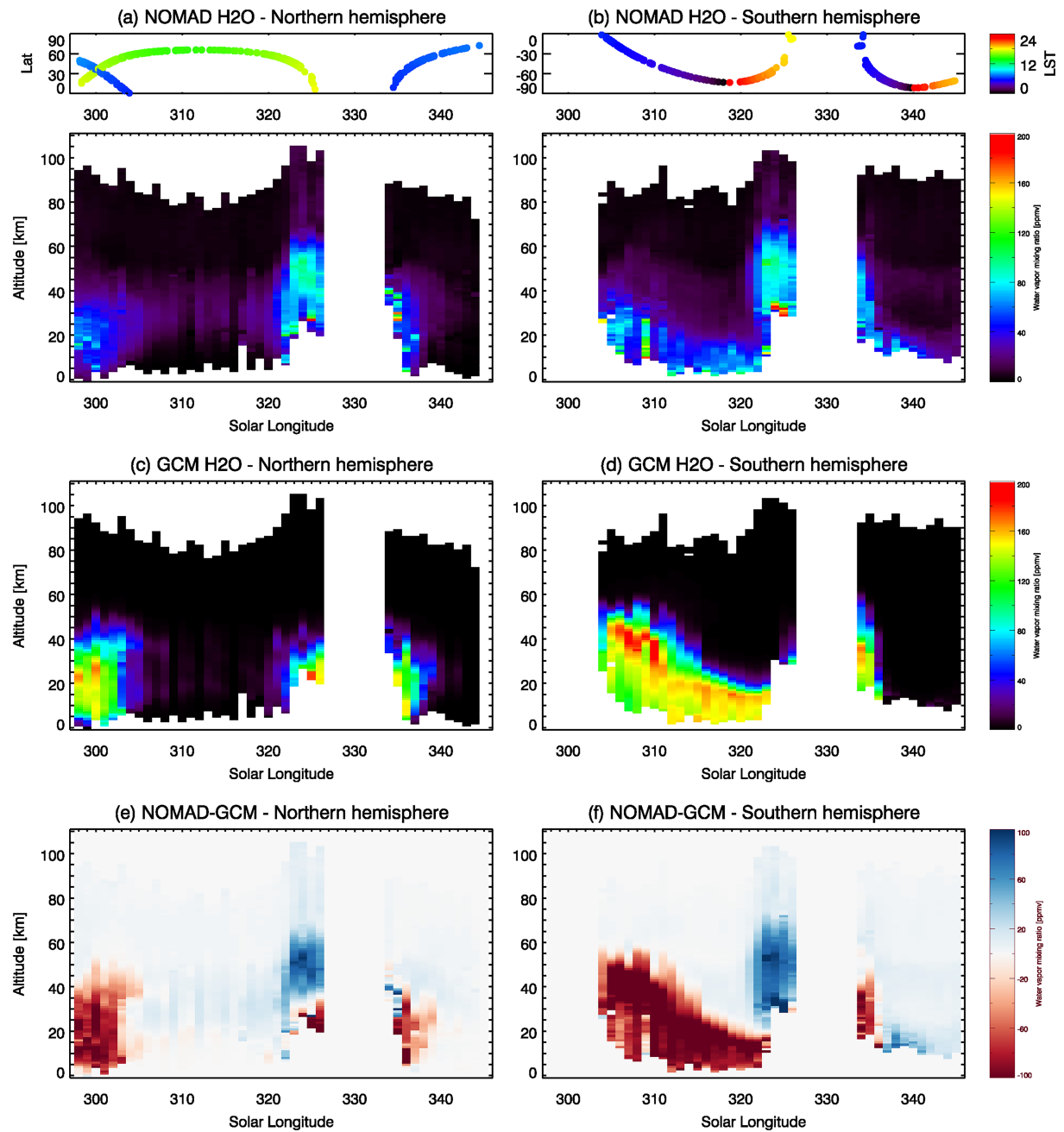
Figure 7. Seasonal variation of the water vapor vertical profiles at $Ls = 298°–345°$ retrieved from the NOMAD data in (a) the Northern Hemisphere and (b) the Southern Hemisphere, (c, d) those predicted by the GEM-Mars for non-dust storm conditions, and (e, f) the differences between the NOMAD retrievals and the GCM predictions. The retrievals and GEM predictions are binned in $1° Ls \times 1$ km altitude grid (averaged in latitude and longitude). The top panels of (a) and (b) show the latitudes and local solar time of the measurements.

(decay phase of the dust storm; Figures 6d and 6e). The latitudinal distributions of the water vapor vertical profiles before and after the onset of the global dust storm are quite different (Figures 6a and 6b). After the onset of the global dust storm, the water vapor abundance in the middle atmosphere is significantly and consistently increased at 60°S–60°N. At the mature phase of the dust storm (Figure 6c), the water vapor abundance is decreased compared to the growth phase; however, the latitudinal distribution of the water vapor is similar. At the growth/mature phase of the dust storm, the season on Mars is just following the northern autumn equinox and it is expected that the Hadley circulation (the equatorial cell) extends to 60° latitude in both hemispheres (e.g., Forget et al., 1999; Takahashi et al., 2003). This explains that the

large water vapor abundance is confined between 60°S and 60°N. Under non-dust storm conditions, water vapor abundances decrease rapidly by ~40 km altitude due to saturation conditions at 30–50 km. Our results suggest that during the dust storm water vapor was transported from the lower to the middle atmosphere by the intensified circulation and expanded above 40 km due to the heating of the middle atmosphere by dust absorption that prevents water vapor from condensation (Neary et al., 2019). In addition, it has been proposed that strong convective transport processes at the mesoscale can create high altitude dust layers (Daerden et al., 2015; Heavens et al., 2018; Spiga et al., 2013; Wang et al., 2018). Such processes will also transport water vapor and may also contribute to the formation of local high-altitude water vapor maxima. At the decay phase of the dust storm (Figures 6d and 6e), the water vapor abundance is similar to that at the mature phase; however, the latitudinal distribution has a gradient with a maximum value at latitudes greater than 60°S. It is well known that the symmetry between two meridional "equinox" cells is significantly reduced at $Ls = 220°$, as the formation of a single pole-to-pole "solstice" Hadley circulation develops (e.g., Forget et al., 1999; Takahashi et al., 2003). The local maximum observed at latitudes greater than 60°S may be explained by a new theoretical study performed by Shaposhnikov et al. (2019). Although their study focused on the MY 28 global dust storm which occurred later in the season ($Ls = 250°–270°$), the authors suggest that transport of water vapor to the upper atmosphere by the strong upward branch of the meridional circulation at perihelion occur only at latitudes greater than 60°S, which corresponds to the location of the peak of water vapor abundances observed by NOMAD.

5. The Regional Dust Storm in 2019

5.1. Overview of the Dust Storm

A 2019 regional dust storm started around 7 January (Ls ~320°) in the Southern Hemisphere, peaked around 15 January, and declined into the middle of February (Ls ~340°) (Chaffin et al., 2019). This seasonal dust event occurs with significantly variable amplitude in every Mars year and can present vertically deep increases in atmospheric temperatures and dust over low to middle latitudes (e.g., Kass et al., 2016), as it did in 2019. As shown in Figure 1b, the measurements by the NOMAD-SO channel cover the whole period of the dust storm except for a gap due to the geometry of the spacecraft's orbit at the active period of this regional dust storm ($Ls = 327°–333°$). The dust top altitude reaches ~50 km in the seasonal range between $Ls = 322°–327°$ in the Southern Hemisphere, which corresponds to the period and the region of the dust storm (reddish colors in Figure 1b).

5.2. Seasonal Variation of the Water Vapor Vertical Profiles

Figures 7a and 7b show the seasonal variation of the water vapor vertical profiles at $Ls = 298°–345°$ retrieved from the NOMAD measurements taken in the Northern Hemisphere (Figure 7a) and Southern Hemisphere (Figure 7b). Figures 7c and 7d show the same water maps as Figures 7a and 7b but simulated by GEM-Mars for non-dust storm conditions (Daerden et al., 2019). Figures 7e and 7f present the differences between the measured water vapor vertical profiles (Figures 7a and 7b) and the predictions by GEM-Mars for non-dust storm conditions (Figures 7c and 7d). In the time before the storm (Ls~300° in the north and Ls~305°–320° in the south) and also at Ls~240°–260° in the Southern Hemisphere (Figure 5b), the GCM water mixing ratios between 10 and 40 km are considerably higher (by a factor ~2) than those measured by NOMAD. However, total water columns from the GCM match very well with observations from TES and CRISM (Daerden et al., 2019; Neary & Daerden, 2018; Smith et al., 2018). This suggests that water vapor was much more confined to the lowest scale height than currently predicted by models. The water vapor abundances in the middle atmosphere suddenly increased around $Ls = 321°$ in both hemispheres and reached maximum values around $Ls = 325°$. The enhancement lasted at least until $Ls = 327°$, before a data gap due to orbital geometry. The GCM data also show a distinct increase of water vapor abundances up to 40 km in this period. However, the increase of water vapor seen in the GCM is due to the latitude of the measurements (low latitudes) and does not expand above 40 km altitude. Since the timing of the enhancement of the water vapor in the middle atmosphere seen by NOMAD corresponds to the period of the regional dust storm and since it expands into the whole middle atmosphere, it is reasonable to attribute that enhancement to the regional dust storm. At the period of this storm, water vapor abundances in the middle atmosphere exceed 150 ppm and water vapor is present up to (at least) 90 km. The water vapor abundances in the middle atmosphere are smaller than those in the 2018 global dust storm and the top altitude is lower.
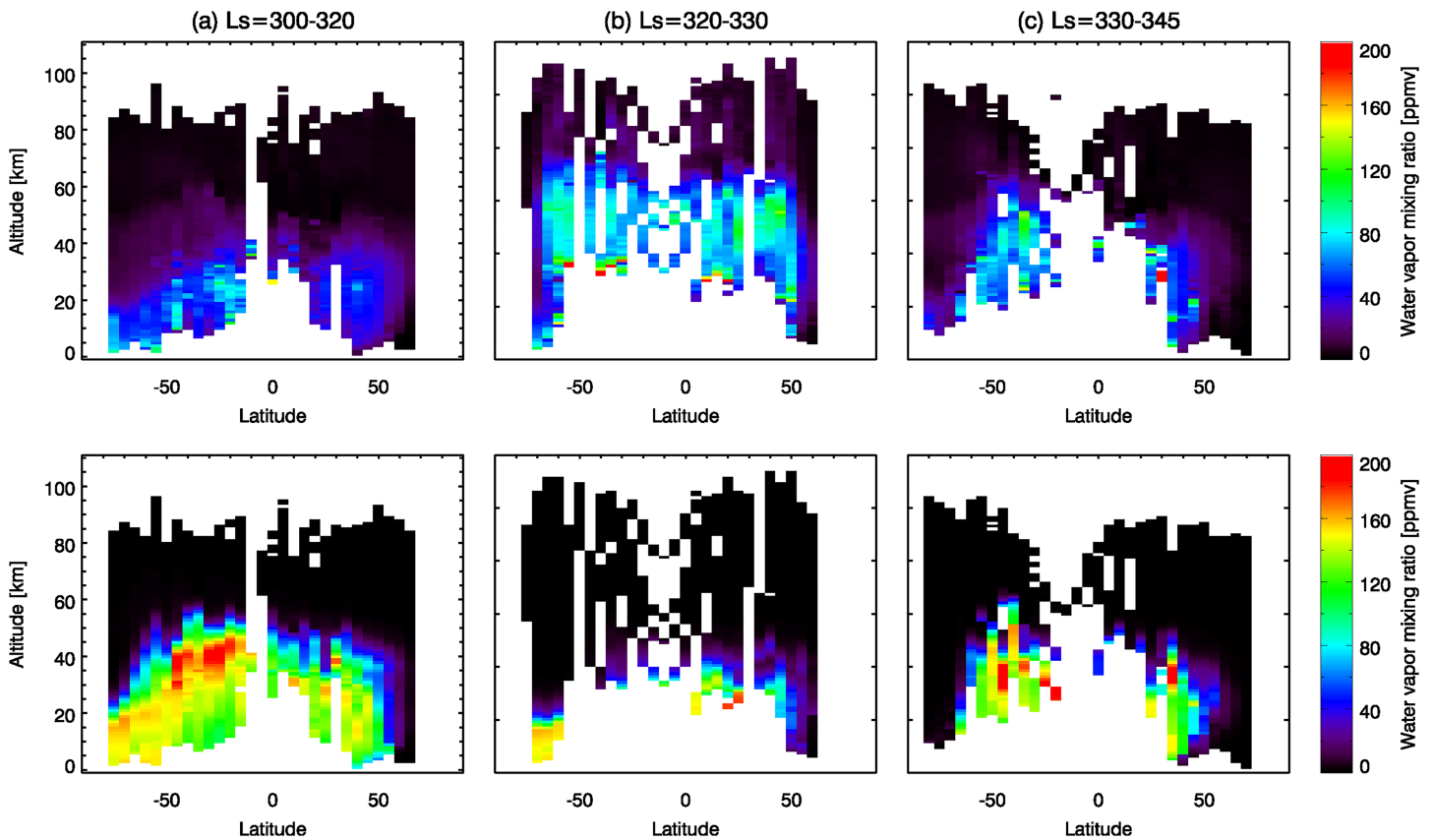
Figure 8. Latitudinal variation of the water vapor vertical profiles retrieved from NOMAD data (the top panels), predicted by the GEM-Mars for non-dust storm conditions (the bottom panels) in the seasonal range between $Ls = 300°–320°$ (a), $Ls = 320°–330°$ (b, at the time of the regional dust storm), and $Ls = 330°–345°$ (c). The retrievals and GEM predictions are binned in 5° latitude × 1 km altitude grid (averaged in season and longitude).

5.3. Latitudinal Variation of the Water Vapor Vertical Profiles

Figure 8 shows the latitudinal map of the water vapor vertical profiles measured by NOMAD and predicted by GEM-Mars for non-dust storm condition at $Ls = 300°–320°$ (Figure 8a), $Ls = 320°–330°$ (Figure 8b, at the time of the regional dust storm), and $Ls = 330°–345°$ (Figure 8c). It is found that the water vapor is significantly increased in the middle atmosphere at the time of the regional dust storm with the maximum values at latitudes greater than 60°S (Figure 8b). The meridional circulation over the period of this regional dust storm ($Ls = 322°–327°$) is still expected to be a single pole-to-pole "solstice" cell. Thus, the mechanism may be the same as for the decay phase of the 2018 global dust storm, that is, the strong upward branch of the meridional circulation, as proposed by Shaposhnikov et al. (2019), may be responsible for the local maximum observed at latitudes greater than 60°S.

6. Conclusions

We have analyzed a selection of the first-year solar occultation measurements by TGO/NOMAD and have presented variations in the vertical profile of water vapor on Mars, including periods of the global dust storm in 2018 and the following regional storm in 2019. The main results are as follows:

1. We find a rapid and significant increase of water vapor in the middle atmosphere following the onset of the global dust storm (around $Ls = 190°$). The enhancement of water vapor at the most active period of the dust storm (around $Ls = 200°$) is remarkable: The water vapor reaches very high altitudes (100 km).
2. The latitudinal variation of water vertical profiles during the growth and mature phases of the global dust storm ($Ls = 196°–202°$ and 210°–220°) shows that the water vapor abundance in the middle atmosphere is consistently increased at 60°S–60°N. The overall increase in middle atmospheric water vapor likely reflects a breakdown in the 30 - 50 km hygropause trapping of water vapor due to dust driven

atmospheric temperature increases. A full simulation in a GCM supporting this explanation is presented in an accompanying paper (Neary et al., 2019).

3. The latitudinal variation of water vertical profiles during the decay phases of the global dust storm ($Ls = 220°$–$240°$ and $240°$–$260°$) shows that the water vapor abundance in the middle atmosphere has peaks at latitudes greater than 60°S. At this time, the global circulation is beginning its transition from an equinoctial to a (southern summer) solstitial Hadley circulation pattern. Strong upward branch of the circulation at latitudes greater than 60°S (Shaposhnikov et al., 2019) may be the responsible for the local maximum.

4. We also find a conspicuous enhancement of water vapor in the middle atmosphere during the regional dust storm in 2019 (around $Ls = 325°$). The magnitude of the water vapor increase is not as large as in the global dust storm but still remarkable: water vapor increases reach ~90 km. Again, this behavior is indicative of dust storm heating conditions.

5. Water vertical profiles observed during this regional dust storm ($Ls = 322°$–$327°$) exhibit peak upper level water vapor abundance at high southern latitudes (60°S), which can be explained by the upward branch of the solstitial Hadley circulation. This annually reoccurring dust storm behavior exhibits strong interannually variability (Kass et al., 2016) and appears to have been particularly intense in this Mars Year (34).

Appendix—The NOMAD team A

Science team: Ann Carine Vandaele, Jose-Juan López-Moreno, Giancarlo Bellucci, Manish R. Patel, Gustavo Alonso-Rodrigo, Shohei Aoki, Francesca Altieri, Sophie Bauduin, David Bolsée, Giacomo Carrozzo, R. Todd Clancy, Edward Cloutis, Matteo Crismani, Frank Daerden, Fabiana Da Pieve, Emiliano D'Aversa, Cédric Depiesse, Justin T. Erwin, Giuseppe Etiope, Anna A. Fedorova, Bernd Funke, Didier Fussen, Maia Garcia-Comas, Anna Geminale, Jean-Claude Gérard, Marco Giuranna, Leo Gkouvelis, Francisco Gonzalez-Galindo, James Holmes, Benoît Hubert, Nicolay I. Ignatiev, Jacek Kaminski, Ozgur Karatekin, Yasumasa Kasaba, David Kass, Armin Kleinböhl, Orietta Lanciano, Franck Lefèvre, Stephen Lewis, Giuliano Liuzzi, Manuel López-Puertas, Miguel López-Valverde, Arnaud Mahieux, Jon Mason, Daniel Mege, Michael J. Mumma, Hiromu Nakagawa, Lori Neary, Eddy Neefs, Robert E. Novak, Fabrizio Oliva, Arianna Piccialli, Etienne Renotte, Birgit Ritter, Séverine Robert, Frédéric Schmidt, Nick Schneider, Giuseppe Sindoni, Michael D. Smith, Nicholas A. Teanby, Ed Thiemann, Ian R. Thomas, Alexander Trokhimovskiy, Loïc Trompet, Jean Vander Auwera, Geronimo L. Villanueva, Sébastien Viscardy, James Whiteway, Valerie Wilquet, Yannick Willame, Michael J. Wolff, Paulina Wolkenberg, Roger Yelle.

Tech. team: Aparicio del Moral Beatriz; Barzin, Pascal; Beeckman, Bram; BenMoussa, Ali; Berkenbosch, Sophie; Biondi, David; Bonnewijn, Sabrina; Candini, Gian Paolo; Clairquin, Roland; Cubas, Javier; Giordanengo, Boris; Gissot, Samuel; Gomez, Alejandro; Hathi, Brijen; Jeronimo Zafra, Jose; Leese, Mark; Maes, Jeroen; Mazy, Emmanuel; Mazzoli, Alexandra; Meseguer, Jose; Morales, Rafael; Orban, Anne; Pastor-Morales, M; Perez-grande, Isabel; Queirolo, Claudio; Ristic, Bojan; Rodriguez Gomez, Julio; Saggin, Bortolino; Samain, Valérie; Sanz Andres, Angel; Sanz, Rosario; Simar, Juan-Felipe; Thibert, Tanguy.

References

Aoki, S., Vandaele, A. C., & Daerden, F., (2019) Vertical profiles of water vapor in the Martian atmosphere during dust storms in 2018–2019 observed by TGO/NOMAD, presented in Aoki et al., JGR. Royal Belgian Institute for Space Aeronomy. https://doi.org/10.18758/71021054

Chaffin, M. S., Chaufray, J.-Y., Stewart, I., Montmessin, F., Schneider, N. M., & Bertaux, J.-L. (2014). Unexpected variability of Martian hydrogen escape. *Geophysical Research Letters*, *41*, 314–320. https://doi.org/10.1002/2013GL058578

Chaffin, M. S., Deighan, J., Schneider, N. M., & Stewart, A. I. F. (2017). Elevated atmospheric escape of atomic hydrogen from Mars induced by high-altitude water. *Nature Geoscience*, *10*(3), 174–178. https://doi.org/10.1038/ngeo2887

Chaffin, M. S., D. M. Kass, S. Aoki, A. A. Fedorova, J. Deighan, J.-Y. Chaufray, et al. (2019), Mars climate controls atmospheric escape: Dust-driven escape from surface to space with MRO/MCS, TGO/NOMAD, TGO/ACS, and MAVEN/IUVS, The Ninth International Conference on Mars abstract #6312.

Clancy, T., Smith, M. D., Lefèvre, F., McConnochie, T. H., Sandor, B. J., Wolff, M. J., et al. (2017). Vertical profiles of Mars 1.27 μm O_2 dayglow from MRO CRISM limb spectra: Seasonal/global behaviors, comparisons to LMDGCM simulations, and a global definition for Mars water vapor profiles. *Icarus*, *293*, 132–156. https://doi.org/10.1016/j.icarus.2017.04.011

Clarke, J. T. (2018). Dust-enhanced water escape. *Nature Astronomy*, *2*(2), 114–115. https://doi.org/10.1038/s41550-018-0383-6

Clarke, J. T., Bertaux, J.-L., Chaufray, J.-Y., Gladstone, G. R., Quemerais, E., Wilson, J. K., & Bhattacharyya, D. (2014). A rapid decrease of the hydrogen corona of Mars: The Martian Hydrogen Corona. *Geophysical Research Letters*, *41*, 8013–8020. https://doi.org/10.1002/2014GL061803

Daerden, F., Neary, L., Viscardy, S., García Muñoz, A., Clancy, R. T., Smith, M. D., et al. (2019). Mars atmospheric chemistry simulations with the GEM-Mars general circulation model. *Icarus*, *326*, 197–224. https://doi.org/10.1016/j.icarus.2019.02.030

Daerden, F., Whiteway, J. A., Neary, L., Komguem, L., Lemmon, M. T., Heavens, N. G., et al. (2015). A solar escalator on Mars: Self-lifting of dust layers by radiative heating. *Geophysical Research Letters*, *42*, 7319–7326. https://doi.org/10.1002/2015GL064892

Fedorova, A., Bertaux, J.-L., Betsis, D., Montmessin, F., Korablev, O., Maltagliati, L., & Clarke, J. (2018). Water vapor in the middle atmosphere of Mars during the 2007 global dust storm. *Icarus*, *300*, 440–457. https://doi.org/10.1016/j.icarus.2017.09.025

Forget, F., Hourdin, F., Fournier, R., Hourdin, C., Talagrand, O., Collins, M., et al. (1999). Improved general circulation models of the Martian atmosphere from the surface to above 80 km. *Journal of Geophysical Research*, *104*(E10), 24,155–24,175. https://doi.org/10.1029/1999JE001025

Gamache, R. R., Farese, M., & Renaud, C. L. (2016). A spectral line list for water isotopologues in the 1100–4100 cm^{-1} region for application to CO$_2$-rich planetary atmospheres. *Journal of Molecular Spectroscopy*, *326*, 144–150. https://doi.org/10.1016/j.jms.2015.09.001

Gordon, I. E., Rothman, L. S., Hill, C., Kochanov, R. V., Tan, Y., Bernath, P. F., et al. (2017). The HITRAN2016 Molecular Spectroscopic Database. *Journal of Quantitative Spectroscopy and Radiative Transfer*, *203*, 3–69. https://doi.org/10.1016/j.jqsrt.2017.06.038

Guzewich, S. D., Lemmon, M., Smith, C. L., Martínez, G., de Vicente-Retortillo, Á., Newman, C. E., et al. (2019). Mars Science Laboratory Observations of the 2018/Mars Year 34 Global Dust Storm. *Geophysical Research Letters*, *46*, 71–79. https://doi.org/10.1029/2018GL080839

Heavens, N., Kleinböhl, A., Chaffin, M. S., Halekas, J. S., Kass, D. M., Hayne, P. O., et al. (2018). Hydrogen escape from Mars enhanced by deep convection in dust storms. *Nature Astronomy*, *2*(2), 126–132. https://doi.org/10.1038/s41550-017-0353-4

Kass, D. M., Kleinboehl, A., McCleese, D. J., Schofield, J. T., & Smith, M. D. (2016). Interannual similarity in the Martian atmosphere during the dust storm season. *Geophysical Research Letters*, *43*, 6111–6118. https://doi.org/10.1002/2016GL068978

Korablev, O., Montmessin, F., Trokhimovskiy, A., Fedorova, A. A., Shakun, A. V., Grigoriev, A. V., et al. (2018). The Atmospheric Chemistry Suite (ACS) of three spectrometers for the ExoMars 2016 Trace Gas Orbiter. *Space Science Reviews*, *214*(1). https://doi.org/10.1007/s11214-017-0437-6

Lemoine, F. G., Smith, D. E., Rowlands, D. D., Zuber, M. T., Neumann, G. A., Chinn, D. S., & Pavlis, D. E. (2001). An improved solution of the gravity field of Mars (GMM-2B) from Mars Global Surveyor. *Journal of Geophysical Research*, *106*(E10), 23,359–23,376. https://doi.org/10.1029/2000JE001426

Liuzzi, G., Villanueva, G. L., Mumma, M. J., Smith, M. D., Daerden, F., Ristic, B., et al., & the NOMAD Team (2019). Methane on Mars: New insights into the sensitivity of CH$_4$ with the NOMAD/ExoMars spectrometer through its first in-flight calibration. *Icarus*, *321*, 671–690. https://doi.org/10.1016/j.icarus.2018.09.021

Maltagliati, L., Montmessin, F., Fedorova, A., Korablev, O., Forget, F., & Bertaux, J.-L. (2011). Evidence of water vapor in excess of saturation in the atmosphere of Mars. *Science*, *333*(6051), 1868. https://doi.org/10.1126/science.1207957

Maltagliati, L., Montmessin, F., Korablev, O., Fedorova, A., Forget, F., Määttänen, A., et al. (2013). Annual survey of water vapor vertical distribution and water-aerosol coupling in the Martian atmosphere observed by SPICAM/MEx solar occultations. *Icarus*, *223*(2), 942–962. https://doi.org/10.1016/j.icarus.2012.12.012

Neary, L., & Daerden, F. (2018). The GEM-Mars general circulation model for Mars: Description and evaluation. *Icarus*, *300*, 458–476. https://doi.org/10.1016/j.icarus.2017.09.028

Neary, L., Daerden, F., Daerden, F., Aoki, S., Whiteway, J., Clancy, R. T., et al. (2019). Explanation for the increase in high altitude water on Mars observed by NOMAD during the 2018 global dust storm. *Geophysical Research Letters*, *46*. https://doi.org/10.1029/2019GL084354

Neefs, E., Vandaele, A. C., Drummond, R., Thomas, I., Berkenbosch, S., Clairquin, R., et al. (2015). NOMAD spectrometer on the ExoMars trace gas orbiter mission: Part 1—Design, manufacturing and testing of the infrared channels. *Applied Optics*, *54*(28), 8494–8520. https://doi.org/10.1364/AO.54.008494

Nevejans, D., Neefs, E., Van Ransbeeck, E., Berkenbosch, S., Clairquin, R., De Vos, L., et al. (2006). Compact high-resolution spaceborne echelle grating spectrometer with acousto-optical tunable filter based order sorting for the infrared domain from 2.2 to 4.3 µm. *Applied Optics*, *45*(21), 5191–5206. https://doi.org/10.1364/AO.45.005191

Rodgers, C. D. (2000). In C. D. Rodgers (Ed.), *Inverse methods for atmospheric sounding—Theory and practice, inverse methods for atmospheric sounding—Theory and practice, Series: Series on Atmospheric Oceanic and Planetary Physics*, ISBN: 9789812813718, (Vol. 2). Singapore: World Scientific Publishing Co. Pte. Ltd., Edited by. https://doi.org/10.1142/9789812813718

Shaposhnikov, D. S., Medvedev, A. S., Rodin, A. V., & Hartogh, P. (2019). Seasonal water "pump" in the atmosphere of Mars: Vertical transport to the thermosphere. *Geophysical Research Letters*, *46*, 4161–4169. https://doi.org/10.1029/2019GL082839

Smith, M. D.Daerden, F.Neary, L.Khayat, S. (2018).The climatology of carbon monoxide and water vapor on Mars as observed by CRISM and modeled by the GEM-Mars general circulation model.*Icarus*, *301*, 117–131. https://doi.org/10.1016/j.icarus.2017.09.027

Spiga, A., Faure, J., Madeleine, J.-B., Määttänen, A., & Forget, F. (2013). Rocket dust storms and detached dust layers in the Martian atmosphere. *Journal of Geophysical Research: Planets*, *118*, 746–767. https://doi.org/10.1002/jgre.20046

Takahashi, Y. O., Fujiwara, H., Fukunishi, H., Odaka, M., Hayashi, Y.-Y., & Watanabe, S. (2003). Topographically induced north-south asymmetry of the meridional circulation in the Martian atmosphere. *Journal of Geophysical Research*, *108*(E3), 5018. https://doi.org/10.1029/2001JE001638

Trompet, L., Mahieux, A., Ristic, B., Robert, S., Wilquet, V., Thomas, I. R., et al. (2016). Improved algorithm for the transmittance estimation of spectra obtained with SOIR/Venus Express. *Applied Optics*, *55*(32), 9275. https://doi.org/10.1364/AO.55.009275

Vandaele, A. C., De Mazière, M., Drummond, R., Mahieux, A., Neefs, E., Wilquet, V., et al. (2008). Composition of the Venus mesosphere measured by Solar Occultation at Infrared on board Venus Express. *Journal of Geophysical Research*, *113*, E00B23. https://doi.org/10.1029/2008JE003140

Vandaele, A. C., Korablev, O., Daerden, F., Aoki, S., Thomas, I. R., Altieri, F., et al., NOMAD Science Team & ACS Science Team (2019). Martian dust storm impact on atmospheric H$_2$O and D/H observed by ExoMars Trace Gas Orbiter. *Nature*, *568*(7753), 521–525. https://doi.org/10.1038/s41586-019-1097-3

Vandaele, A. C., Kruglanski, M., & De Maziere, M. (2006). Simulation and retrieval of atmospheric spectra using ASIMUT, paper presented at Atmospheric Science Conference, Eur. Space Agency, Frascati, Italy.

Vandaele, A. C., Lopez-Moreno, J.-J., Patel, M. R., Bellucci, G., Allen, M., Alonso-Rodrigo, G., et al., & the NOMAD Team (2018). NOMAD, an integrated suite of three spectrometers for the ExoMars Trace Gas mission: technical description, science objectives and expected performance. *Space Science Reviews*, *214*(5). https://doi.org/10.1007/s11214-018-0517-2

Vandaele, A. C., Mahieux, A., Robert, S., Berkenbosch, S., Clairquin, R., Drummond, R., et al. (2013). Improved calibration of SOIR/Venus Express spectra. *Optics Express*, *21*(18), 21,148–21,161. https://doi.org/10.1364/OE.21.021148

Wang, C., Forget, F., Bertrand, T., Spiga, A., Millour, E., & Navarro, T. (2018). Parameterization of rocket dust storms on Mars in the LMD Martian GCM: Modeling details and validation. *Journal of Geophysical Research: Planets*, *123*, 982–1000. https://doi.org/10.1002/2017JE005255